nature communications

Article

https://doi.org/10.1038/s41467-026-69499-6

Interfacial stress decoupling enables stable palladium-based hydrogen sensing

Received: 21 May 2025

Accepted: 30 January 2026

Published online: 12 February 2026

Check for updates

Rui Gao[1,2,3], Guozhu Zhang[1,2,3] ✉, Xiaoyuan Wang[1,2,3], Yujing Xu[1,2,3], Chao Zhang[1,2,3], Linfeng Li[1,2,3], Zeyu Wang[1,2,3], Bowei Zhang[1,2,3], Kazuki Nagashima[4,5], Takeshi Yanagida[6,7] & Fu-Zhen Xuan[1,2,3] ✉

Interfacial adhesion between the sensing layer and supporting substrate critically governs the long-term stability of electrical molecular sensors. However, achieving a robust heterointerface remains challenging due to the intrinsic lattice mismatch induces localized stress, which is further exacerbated by cyclic interactions between the sensing film and gas analytes. Here, we introduce a floating-structure palladium hydrogen (H_2) sensor enabled by interfacial stress decoupling through a dithiol-based self-assembled monolayer (SAM). This interfacial layer acts as a molecular bridge between the palladium sensing layer and the substrate electrode, forming a dual-interface architecture that simultaneously mitigates the interfacial stress and suppresses the substrate clamping effects, thereby accelerating H_2 absorption kinetics. The resulting sensor demonstrates a stable and cyclable H_2 detection at concentrations up to 4 vol%, and an ultrasensitive detection limit of 1 ppm at room temperature. Moreover, we realize wafer-scale fabrication and integration of the sensor into a portable platform for real-time hydrogen leak detection. This interfacial stress-engineering approach provides a general route toward durable and high-performance molecular sensor.

Robust heterogeneous interfaces are essential for integrating modern electronic devices[1–4], particularly electrical molecular sensors, where strong adhesion between the sensing layer and substrate prevents delamination and ensures long-term acquisition of chemical information[5–7]. However, constructing durable heterointerfaces remains challenging because intrinsic lattice mismatches produce localized stress that is further exacerbated by gas–material interactions such as H_2 adsorption. As a clean energy carrier with a high gravimetric energy density, H_2 plays a pivotal role in the global transition toward carbon-neutral energy systems[8,9]. While its flammability and low ignition energy demand highly sensitive, rapid, and reliable detection methods for safety-critical applications[10–12]. Among the various strategies for hydrogen detection, electrical sensors based on Pd nanostructures have attracted considerable interest due to their exceptional H_2-specific absorption properties and the resulting measurable changes in electronic conductivity[13–15]. Yet, despite their high sensitivity and selectivity, the long-term operational reliability of Pd-based sensors remains a grand challenge. This is primarily due to the inherent phase transition between Pd and PdH_x during cyclic H_2 absorption/desorption, which induces repetitive lattice expansion and contraction[16,17]. Over prolonged operation, this leads to microstructural degradation, including stress accumulation, dislocation generation, and grain boundary embrittlement, which ultimately lead to delamination or fracture[18,19]. This degradation in turn weakens the

[1]Shanghai Key Laboratory of Intelligent Sensing and Detection Technology, Shanghai, PR China. [2]School of Mechanical and Power Engineering and, East China University of Science and Technology, Shanghai, PR China. [3]Key Laboratory of Pressure Systems and Safety of Ministry of Education, East China University of Science and Technology, Shanghai, PR China. [4]Graduate School of Chemical Science and Engineering, Hokkaido University, Sapporo, Hokkaido, Japan. [5]Research Institute for Electronic Science, Hokkaido University, Sapporo, Hokkaido, Japan. [6]Department of Applied Chemistry, Graduate School of Engineering, The University of Tokyo, Bunkyo, Tokyo, Japan. [7]Institute for Materials Chemistry and Engineering, Kyushu University, Kasuga, Fukuoka, Japan. ✉e-mail: gz_zhang@ecust.edu.cn; fzxuan@ecust.edu.cn

interfacial adhesion between the Pd layer and substrate, critically undermining device durability. To address this challenge, robust heterogeneous interfaces are strongly needed that can endure cyclic mechanical deformation while maintaining high sensitivity.

The central challenge in fabricating these gas sensor interfaces lies in achieving a combination of high interfacial strength to prevent delamination and adequate toughness to accommodate stress from H_2-induced lattice transformations without brittle fracture. Conventional approaches to enhance interfacial adhesion include chemical functionalization[20], adhesion-promoting polymer integration[7], and substrate roughening[21,22]. These methods operate via mechanisms such as increasing interfacial surface energy, introducing chemical bonding sites, or enabling mechanical interlocking. For instance, titanium (Ti) buffer layers have been introduced to suppress Pd phase transitions[23], while polymers like polydopamine have been shown to promote interfacial bonding[24]. Nevertheless, these strategies often exacerbate the substrate clamping effect, wherein rigid bonding inhibits hydrogen diffusion into the Pd layer[23,25], thereby degrading response time and sensitivity. Moreover, interfacial stress accumulation arising from intrinsic material-molecule interactions still remains unsolved. To overcome these limitations, recent studies have employed flexible substrates, such as PDMS or other elastomers, to provide stress-buffering effects through their intrinsic stretchability[17]. By accommodating volumetric changes during H_2 adsorption, these materials reduce interfacial delamination and prolong sensor lifespan. However, Pd layers deposited onto elastomers are typically bonded via weak van der Waals or electrostatic forces[26,27], which are insufficient to ensure long-term mechanical stability under cyclic operations. Therefore, there is an urgent need for advanced heterointerfaces that not only enhance mechanical adhesion but also accommodate structural changes induced by H_2 absorption. Such interfaces must regulate hydrogen transport kinetics while dissipating stress from lattice expansion, thereby enabling the development of durable, high-performance Pd-based H_2 sensors.

Herein, we introduce a floating-structure H_2 sensor that bridges the Pd sensing layer and the substrate electrode with the molecular dithiol SAM, forming a stress decoupling heterointerface. In contrast to conventional interfaces held together by weak van der Waals forces, our integrated heterointerface is reinforced by robust sulfur-metal coordination and a flexible carbon backbone, which significantly improves mechanical toughness and interface stability. This dual-interface design simultaneously mitigates interfacial stress and suppresses substrate clamping effects, thereby accelerating H_2 absorption kinetics. As a result, the sensor exhibits a stable and cyclable H_2 detection at concentrations up to 4 vol%, and an ultrasensitive detection limit of 1 ppm at room temperature. Furthermore, we realized wafer-scale fabrication of floating-structure H_2 sensors and integrated them into a portable detection system for practical hydrogen leak detection. Collectively, this work establishes a design paradigm for molecular sensing interfaces, overcoming the trade-off between sensitivity and mechanical durability and providing a scalable foundation for next-generation chemical sensors with extended lifetimes and enhanced reliability.

Results

Design concept of dithiol SAM-engineered heterointerfaces for H_2 gas sensor integration

To ensure that the introduction of a SAM layer does not compromise the adsorption-absorption kinetics of the hydrogen molecules on Pd sensing layer during hydrogen detection, a floating-structure design of Pd-based H_2 sensor is proposed here (Fig. 1a). The fabrication process consists of three key steps: (i) deposition of a stable gold (Au) bottom electrode film on the substrate, (ii) growth of a SAM interlayer to optimize interfacial bonding, and (iii) deposition of the Pd sensing layer onto the SAM surface to ensure H_2 adsorption-desorption behavior unaffected by the interfacial layer during gas sensing. Regarding SAM molecule selection (Fig. 1c), we formed the SAM using dithiol-terminated molecules with either alkyl or π-conjugated benzene backbones (Supplementary Fig. 1). This molecular structure enables dual interfacial chemical bonding: on one side, the thiol (-SH) group forms a covalent Au-S bond with the gold electrode, while on the other, the terminal sulfur atom coordinates with the Pd sensing layer via Pd-S interactions, thereby enhancing interfacial adhesion and improving sensor stability. Furthermore, the innovative aspect of this structure lies in the mechanical buffering effect of the SAM layer (Fig. 1d). As is known, the sensing mechanism of the Pd-based hydrogen sensor primarily relies on the lattice expansion induced by hydrogen absorption[16,28,29]. As H_2 molecules dissolve into the Pd lattice, the lattice parameter and unit cell volume increase proportionally, exhibiting a linear expansion trend (Fig. 1e). Simultaneously, as the H_2 dissolution concentration varies, Pd undergoes a phase transition between α-PdH_x and β-PdH_x. Owing to the distinct electrical resistivity of Pd and PdH_x, real-time monitoring of the electrical signal variations in the Pd sensing film enables quantitative detection of H_2 concentration in the environment[14,30]. Additionally, the carbon backbone of the SAM imparts mechanical flexibility, allowing the layer to expand and contract in response to Pd lattice changes during H_2 adsorption and absorption. This adaptability effectively buffers the mechanical stress, mitigating both lateral shear and longitudinal compressive strains induced by Pd lattice expansion and contraction (Fig. 1d). Such stress-buffering capacity is key to enhancing the long-term stability and operational reliability of the sensor. Meanwhile, theoretical calculations (Fig. 1f) reveal that the bonding energies of S-Pd (−2.85 eV) and S-Au (−1.92 eV) are substantially higher than that of Pd-Au (−1.15 eV), where Pd is directly deposited on the gold electrode. These results demonstrate that the introduction of dithiol SAM interlayer significantly enhances the adhesion between the Pd sensing layer and the Au electrode, thereby reducing interfacial delamination risk. Consequently, the floating-structure Pd-based H_2 sensor, through synergistic optimization of interfacial engineering and micromechanical design, presents a robust solution to the persistent issues of interfacial failure and stress accumulation, thereby paving the way for highly stable and durable hydrogen sensing technologies.

SAM-engineered H_2 sensor fabrication and performance

Figure 2a and Fig. 2b show a schematic illustration and corresponding optical images of the fabricated floating-structure sensor device integrated with a dithiol SAM layer. Detailed fabrication procedures are provided in the Experimental Section and schematically presented in Supplementary Fig. 2. In contrast to conventional planar sensor designs, where parallel-patterned electrodes on a substrate are subsequently coated by a sensing film (Supplementary Fig. 3), our device utilizes a vertically aligned crossbar architecture. In this design, two vertically stacked electrodes are separated by a dithiol SAM layer and a Pd sensing film, enabling full circumferential exposure to enhance hydrogen detection performance. To avoid electrical short-circuiting between the lower Au electrode and the upper Pt electrode, a SiO_2 insulation layer was deposited over the Au electrode, leaving only a 200 μm circular window for selective SAM formation. A cross-sectional schematic of the sensor structure is provided in Fig. 2c. Considering that the thicknesses of the dithiol SAM and Pd sensing layer critically affect both mechanical stability and hydrogen detection sensitivity, these parameters were systematically optimized by tuning the SAM layer growth time and Pd film deposition thickness. The crystallographic orientation of the deposited Pd film was characterized by X-ray diffraction (XRD), confirming a cubic structure with a preferential (111) orientation (Fig. 2d). Scanning electron microscopy (SEM) imaging (inset of Fig. 2d and Supplementary Fig. 5) further demonstrates the formation of a uniform, densely packed Pd film with a thickness of approximately 80 nm.

https://doi.org/10.1038/s41467-026-69499-6

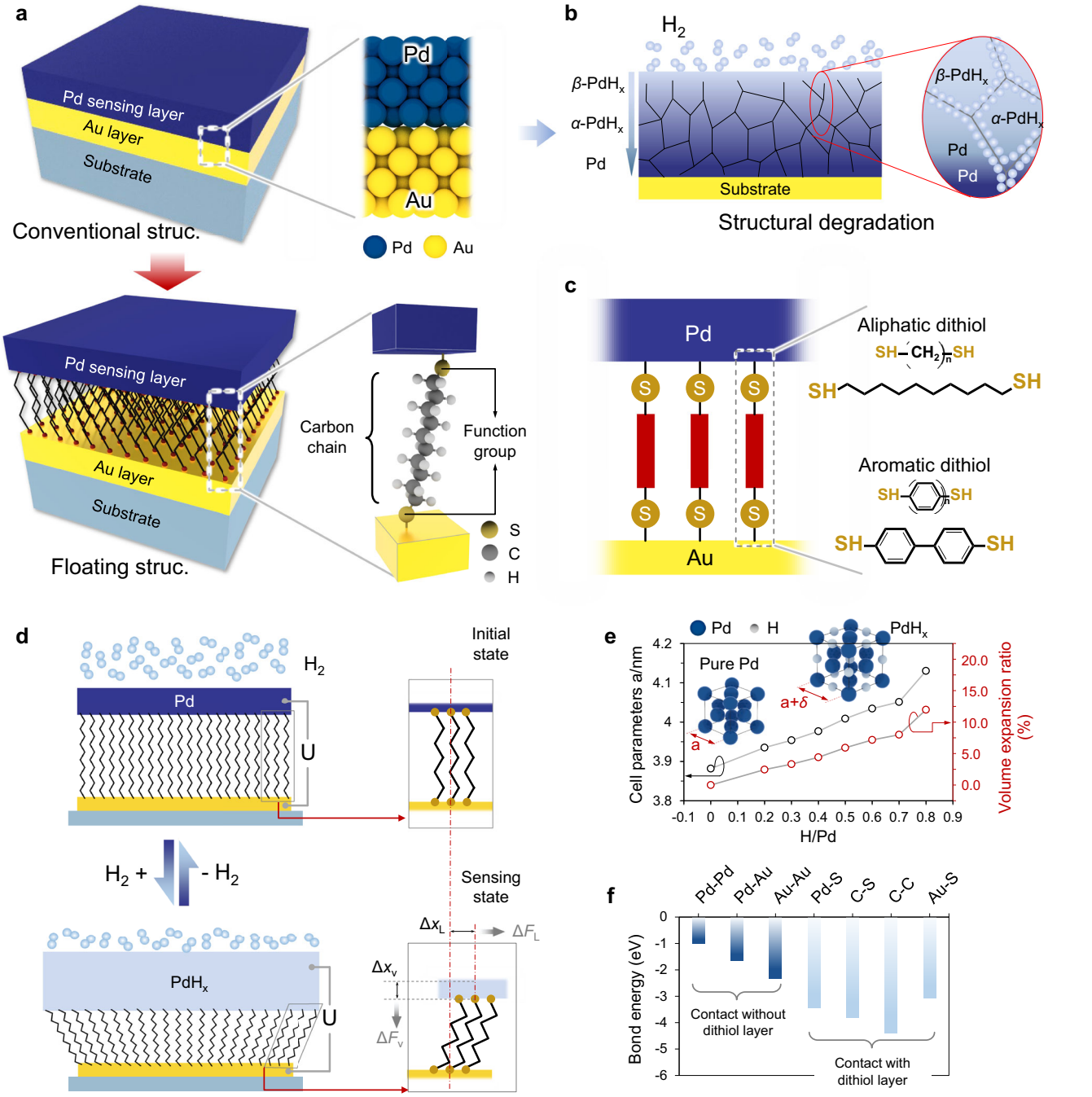

Fig. 1 | Design concept of dithiol SAM-engineered heterogeneous interfaces for H_2 gas sensor integration. a Schematic comparison of conventional planar-structured and proposed floating-structured Pd-based H_2 sensors. **b** Illustration of structural degradation in a conventional planar-structured Pd film under repeated H_2 absorption/desorption cycles. **c** Molecular structure of the SAM buffer layer composed of dithiol molecules with alkyl chains and benzene-ring moieties. **d** Mechanistic model illustrating interfacial stress dissipation in the dithiol-SAM-engineered floating-structured Pd-film H_2 sensor. **e** Volumetric expansion and lattice parameter evolution of Pd during palladium hydride (PdH_x) formation. **f** Comparative bond energy analysis between sulfur (S) and palladium (Pd), gold (Au), or carbon (C). Struc. structure. Source data are provided as a Source Data file.

To verify the incorporation of the dithiol self-assembled monolayer (SAM), cross-sectional high-resolution transmission electron microscopy (HRTEM) combined with energy-dispersive X-ray spectroscopy (EDX) mapping and line profiling was conducted on the Pd–SAM–Au junction within the sensor device (Fig. 2e–g). Here the incorporated dithiol SAM molecule is 1,10-decanedithiol (C10). HRTEM analysis reveals a uniform interfacial layer (~2 nm) in intimate contact with both Pd and Au, with a thickness consistent with the theoretical molecular length of C10 (Supplementary Fig. 1), confirming successful SAM integration in the floating structure. Notably, due to the use of RF sputtering for Au deposition, the resulting Au films exhibited a nanodot morphology (Supplementary Fig. 4), potentially allowing partial penetration of dithiol molecules into the Au layer. Such a structural configuration facilitates the formation of a continuous SAM across the nanodot surfaces, as evidenced by sulfur distribution in the EDX elemental mapping and line scan (Fig. 2f and 2g), which confirms sulfur presence throughout the Au region. Furthermore, the chemical interactions between the C10 and the Pd and Au were investigated using X-ray photoelectron spectroscopy (XPS) (Fig. 2h and Supplementary Fig. 6 and Fig. 7). The XPS analysis reveals distinct sulfur–metal binding

https://doi.org/10.1038/s41467-026-69499-6

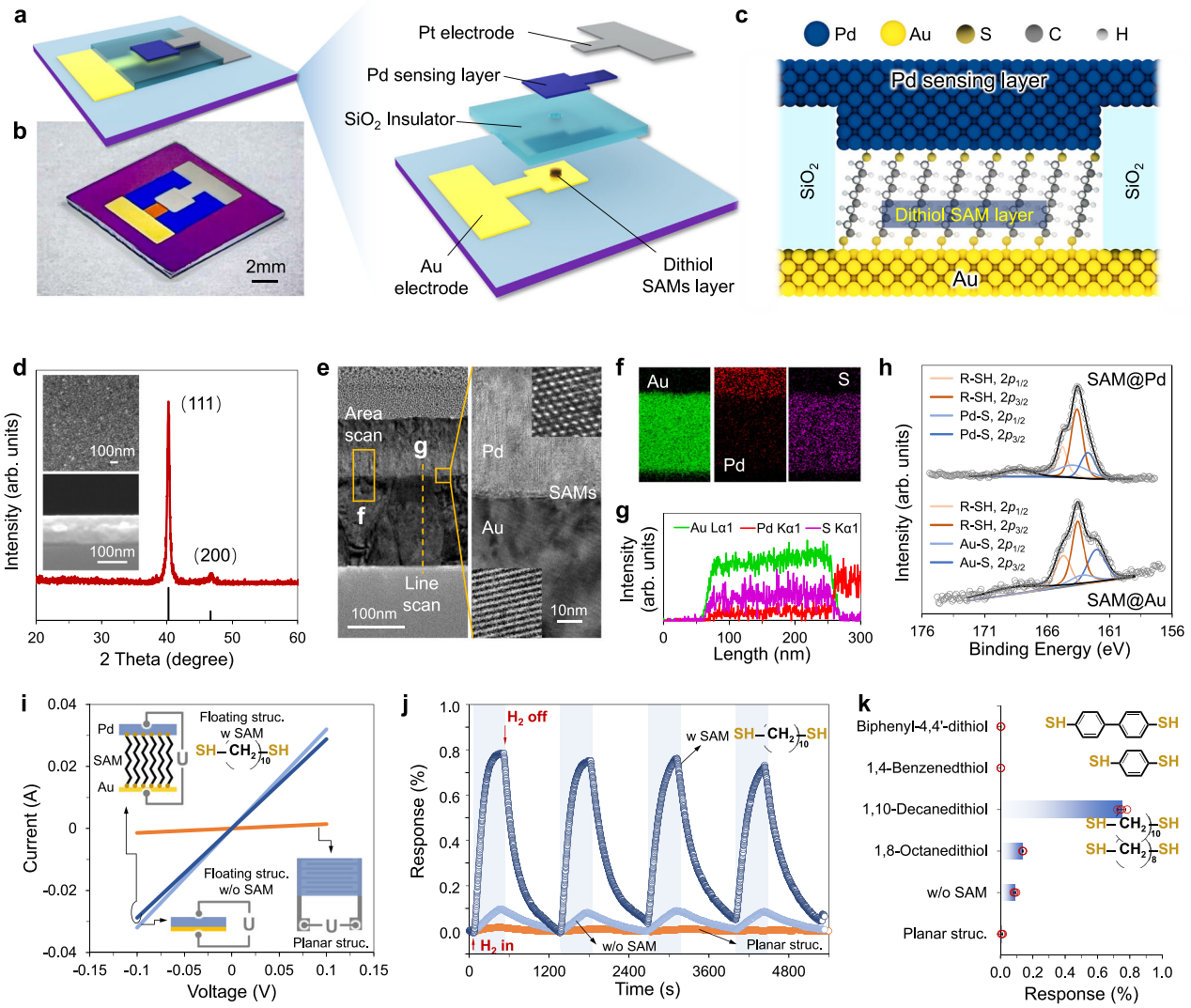

Fig. 2 | Fabrication and performance evaluation of floating-structured Pd-film-based H_2 sensors. a Schematic illustration of the floating-structured Pd H_2 sensor design with an embedded dithiol SAM buffer layer. **b** Optical image of the as-fabricated floating-structured Pd-film-based H_2 sensor device. **c** Cross-sectional schematic illustrating the interfacial Pd-SAM-Au interfacial heterostructure. **d** SEM micrograph and XRD pattern of deposited Pd sensing layer. Top-view and cross-sectional micrographs of Pd films obtained from three independent experiments. **e** Cross-sectional TEM image of the Au-SAM-Pd heterostructure functionalized with 1,10-decanedithiol molecules. Each micrograph obtained similar results in three independent experiments. **f** Elemental mapping analysis and (**g**) EDS line-scan profile of the Au-SAM-Pd structure shown in (**e**). **h** XPS of 1,10-decanethiol SAM layer grown on Pd and Au surface. **i** Comparative I-V curves for planar-structured and floating-structured Pd-film-based sensor devices. **j** Real-time response curves of planar and floating sensor devices exposed to 1000 ppm H_2 at room temperature. **k** Comparative H_2 (1000 ppm) response histograms of floating-structured devices incorporating different SAM buffer layers ($n = 4$). n represents the number of technical independent replicates. The error bars represent the standard deviation of four repeated sensing cycles measured on a single sensor device. Each micrograph obtained similar results in three independent experiments. Struc. structure, w with, w/o without. Source data are provided as a Source Data file.

peaks for both Pd (S–Pd: $2p_{3/2} = 164.0$ eV, $2p_{1/2} = 162.7$ eV)[31,32] and Au (S–Au: $2p_{3/2} = 163.1$ eV, $2p_{1/2} = 162.0$ eV)[33,34], confirming the chemisorption of thiol groups. Additionally, another set of sulfur satellite peaks which attributed to unbound –SH termini is observed in both the SAM-Pd (164.8 eV and 162.7 eV)[35] and SAM-Au (164.7 eV and 162.7 eV)[34] spectra, which further support the formation of a well-aligned, ordered SAM without disordered growth.

Furthermore, the electrical and hydrogen sensing performance of the SAM-engineered sensor devices was systematically investigated. Figure 2i presents the I-V characteristics of three different sensor architectures: conventional planar structure (Supplementary Fig. 8), a floating structure without a SAM layer, and a floating structure incorporating a C10 SAM layer. A detailed analysis of the conduction characteristics for floating-structured devices with different dithiol SAM is presented in Supplementary Fig. 8. The results indicate that the sputtered Pd film exhibits higher conductivity in the vertical direction compared to the lateral direction. Notably, a slight decrease in conductivity is observed upon the introduction of the dithiol SAM, suggesting that although the SAM introduces a heterointerface, efficient charge transport is still maintained. Subsequently, H_2 sensing performance was further evaluated under 1000 ppm H_2 at room temperature (Fig. 2j and Supplementary Fig. 9 and Fig. 10). It is seen that the planar structure device presents a very tiny sensing response (Supplementary Fig. 9), while the SAM-integrated floating structure demonstrated a gigantic sensing performance improvement over the planar and SAM-free floating structure. Moreover, the influences of SAM growth time and Pd film thickness on sensing sensitivity, response time, and recovery characteristics were also systematically assessed

(Supplementary Fig. 11 and Fig. 12). Due to the SAM layer growth on metals surfaces proceeds via rapid initial diffusion-limited chemisorption, followed by slower two-dimensional nucleation and molecular reorganization into densely packed, ordered films[36], the growth time critically influences the orientation characteristics and film qualities of SAM layer. Thus, the optimized SAM growth time for such a sensor architecture design was determined with 24 h. Under these conditions, a Pd film thickness of ~80 nm exhibited the highest H_2 sensitivity and optimal response/recovery dynamics (Supplementary Fig. 12). Furthermore, the H_2 sensing performance of floating-structured sensors incorporating various dithiol SAM was evaluated (Fig. 2k and Supplementary Fig. 10). The results reveal that aliphatic dithiol SAM composed of aliphatic dithiols, characterized by flexible alkyl chains, markedly enhance sensor sensitivity, with performance progressively increasing with chain length. In contrast, aromatic dithiol SAM produced a dendritic effect that adversely impacted the sensing response. This degradation is primarily caused by the rigid π-conjugated backbone of the aromatic molecules. This structural property first prevents tight molecular packing and then facilitates dendritic growth during film formation. Ultimately, these defects disrupt the interface uniformity[37,38], hindering electron transport across the sensing junction. These findings highlight the pivotal role of interface engineering using aliphatic dithiol SAM layer in floating-structure designs for promoting H_2 adsorption.

Sensing mechanisms of SAM-engineered H_2 sensor

To elucidate the mechanism by which the C10 SAM layer enhances H_2 sensing, we systematically investigate interfacial electron transport across the Pd-SAM-Au junction, which is regarded as a critical factor governing sensing performance. To this end, ultraviolet photoelectron spectroscopy (UPS) and current–voltage (I–V) measurements are employed to characterize the interfacial electronic structure and its correlation with H_2-induced dynamic responses of the Pd layer.

Alkyl-chain thiol molecules, terminated with reactive –SH groups, readily form strong chemisorption bonds with noble metals such as Au and Pd, enabling the fabrication of robust and tunable molecule–electrode interfaces[32,39]. Their extended alkyl chains spontaneously organize into highly ordered SAM layer, allowing precise structural control in nanoscale electronic architectures. Owing to these characteristics, such molecules are widely employed in molecular-scale electronic devices, including switches and transistors[40–42]. In this study, we focus on C10, a saturated σ-bonded molecule exhibiting a wide HOMO–LUMO energy gap (Fig. 3a and Supplementary Fig. 18), which renders it electrically insulating in the absence of metal coupling. However, upon adsorption onto metal surfaces (Au or Pd), the end-group of thiol (-SH) usually form covalent S–metal bonds, inducing substantial interfacial electron coupling and energy-level realignment. This interaction leads to the formation of interfacial states near the Fermi level, indicative of Fermi-level pinning effects that modulate the local electronic structure and facilitate charge transport[43–45]. UPS measurements (Fig. 3b and 3c) reveal a pronounced decrease in work function following SAM adsorption, suggesting the formation of interfacial dipoles driven by S–metal bonding. The resulting energy-level reordering reduces the charge injection barrier, thereby enhancing electron transmission across the interface[43,46]. This phenomenon is further supported by first-principles calculations, which predict improved energy-level alignment and enhanced interfacial conductivity (Fig. 3e and Supplementary Fig. 19). Notably, coordination of the C10 molecule with Pd and Au induces the emergence of new electronic states near the Fermi level in the Pd–SAM–Au system, indicating strong interfacial electronic coupling that facilitates charge transport across the heterojunction[47–49]. To further assess the electron transport capability of the SAM layer during H_2 response process, we simulated density of states (DOS) variations in the Pd–SAM–Au system under applied uniaxial strains ranging from 1% to 10% (Fig. 3e and Supplementary Fig. 20). The results show a progressive increase in DOS for energy states above the Fermi level ($E-E_F > 0$) with increasing strain, indicating electron transport at the interface is further enhanced under mechanical stress. In addition, the PDOS results reveal that the Pd-*d* and Au-*d* orbitals exhibit minimal variation under compressive strain (Supplementary Fig. 21 and Fig. 22). In contrast, the S-*p* states show notable redistribution, particularly near the Fermi level. This selective modulation suggests that strain primarily influences the electronic states localized at the Pd–SAM–Au interface, rather than altering the bulk electronic structure of the metal layers. The observed change in S-*p* PDOS under strain indicates a strain-induced modification in the orbital hybridization between S and the adjacent Pd and Au layers. As the interface undergoes mechanical compression (mimicking the effect of hydriding-induced lattice stress), the overlap between S-*p* and metal *d*-orbitals is enhanced, which in turn can facilitate improved charge transport across the interface. In this context, charge transport across the heterojunction can be understood as electron tunneling through a potential barrier. Additionally, complementary I–V measurements were performed to evaluate charge transport behavior experimentally (Fig. 3f). The corresponding Fowler–Nordheim (F–N) plot of $\ln(I/V^2)$ versus $1/V$ shows linear behavior across a wide voltage range, suggesting ohmic conduction with no discernible transition voltage even under high bias. This observation is consistent with a stable off-resonant transport regime[43,50]. These results indicated that, despite the formation of new electronic states following thiol coordination with Pd and Au, the heterointerface still remains remarkable electron transport properties (Fig. 3g). Collectively, these findings highlight that the introduction of the thiol SAM not only preserves the intrinsic conductive properties of the heterojunction interface but also enhances electron transport via interfacial stress transfer induced by hydrogen adsorption in the Pd film.

Furthermore, the influence of the SAM layer on H_2 adsorption kinetics during the sensing process was investigated. In metallic Pd, H_2 adsorption proceeds via surface molecular adsorption and dissociation, followed by the diffusion of dissociated atomic hydrogen into the Pd bulk, where it occupies interstitial lattice sites to form palladium hydride[51,52] (Fig. 3h). The extent of hydrogen absorption is quantitatively described by the bulk hydrogen-to-palladium atomic ratio (H/Pd, denoted as n), which governs the phase transition from metallic Pd to the hydride phase. However, in the sensor architecture presented here, where the Pd film is deposited on a substrate, hydrogen diffusion into the bulk is constrained by mechanical clamping from the substrate[53–55]. This restriction limits volumetric expansion and thereby suppresses further hydrogen absorption until an equilibrium is established between bulk expansion and substrate-induced confinement (Fig. 3h). Consequently, the hydriding process in thin Pd films follows a nonlinear kinetic regime, defined by a dynamic equilibrium between lattice Pd and absorbed hydrogen[51]. This regime also corresponds to the phase during which the sensor gradually reaches maximum performance in its dynamic electrical response (Fig. 2j). To quantify the real-time H/Pd ratio in bulk Pd, an essential parameter for evaluating the SAM layer's role in tailoring H_2 absorption, we analyzed the temporal evolution of the $n(t)$ within the bulk diffusion regime (Fig. 3i). These values were extracted from dynamic hydrogen response curves (Fig. 2j). The time scale was adjusted so that $t = 0$ s marks the onset of the nonlinear regime. Details of the calibration procedure are provided in the Supplementary (Section VI, H_2 absorption modeling). The solid lines in Fig. 3i represent fits obtained using absorption-related kinetic models for the bulk diffusion regime[51].

$$n(t) = -\frac{C_2}{C_1} + \left(n_0 + \frac{C_2}{C_1}\right)\exp(C_1(t - t_0)) \quad (1)$$

https://doi.org/10.1038/s41467-026-69499-6

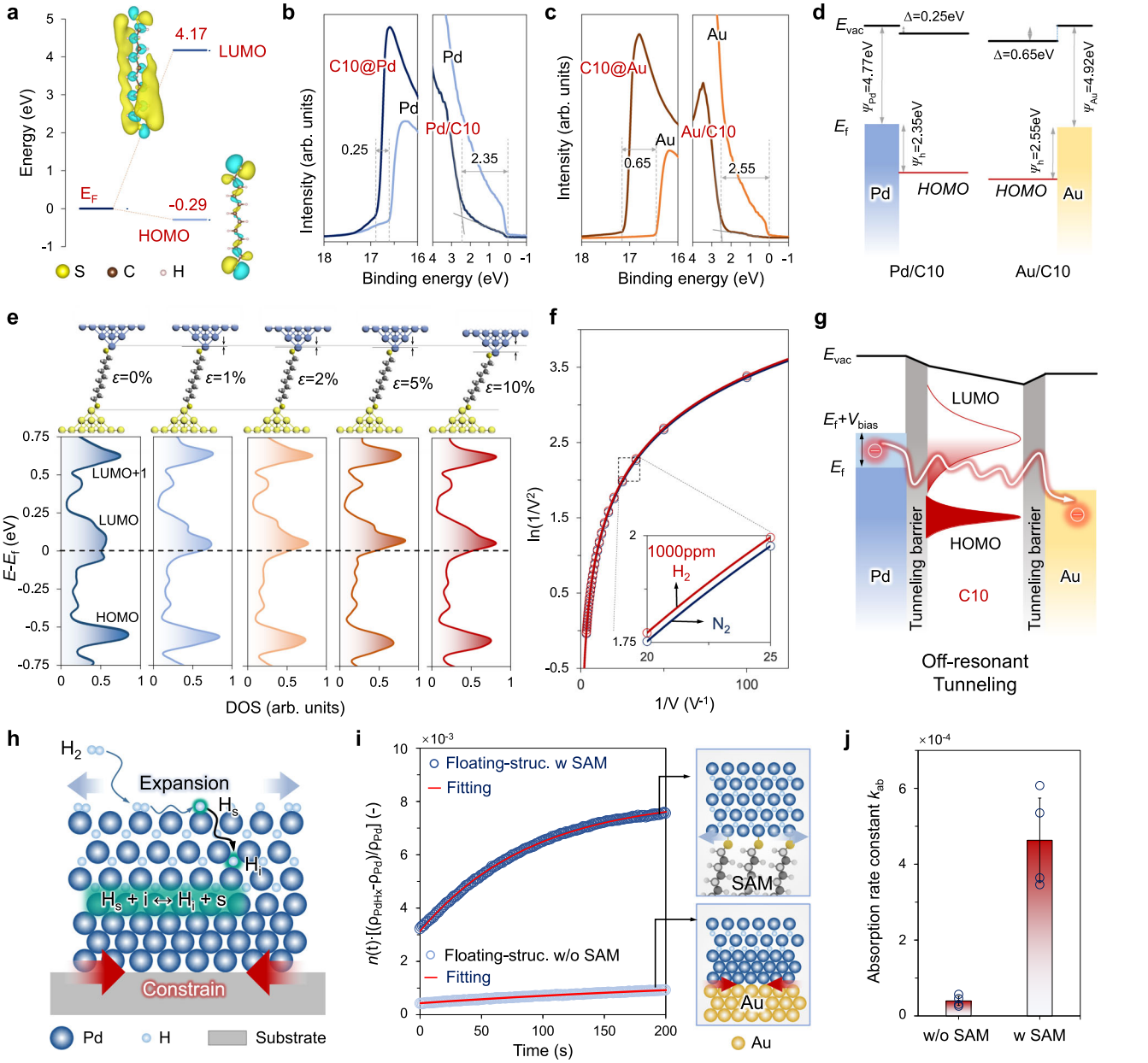

Fig. 3 | Electron transport and H_2 sensing mechanisms in floating-structured Pd-film-based sensor devices. a Calculated electronic energy level distribution of the C10 molecule. **b**, **c** UPS spectra of C10 SAM layer grown on Pd and Au films, respectively. **d** Energy band alignment diagram for the Pd/C10/Au interfacial heterostructure. **e** DOS profiles for the Pd-SAM-Au system under compressive strains of $\varepsilon = 0\%$, 1%, 2%, 5%, and 10%. **f** Differential I-V curves of the sensor device under 0 ppm and 1000 ppm H_2. **g** Proposed electron tunneling mechanism across the Pd-SAM-Au floating heterostructure. **h** Schematic illustration of the key kinetic steps involved in Pd hydride formation during H_2 sensing. **i** Evolution of the bulk hydrogen-to-palladium atomic ratio (n) in nonlinear kinetic regimes for sensors with and without the C10 SAM layer. Solid lines represent fits to Eq. (1). **j** Extracted hydrogen absorption rate constants derived from the data in (**i**) ($n = 4$). n represents the number of technical independent replicates. The error bars represent the standard deviation of four repeated sensing cycles measured on a single sensor device. Struc. structure, w with, w/o without. Source data are provided as a Source Data file.

$$C_1 = -k'_{ab}\left(1 + \frac{K_s}{\sqrt{p_{H2}}}\right)$$
$$C_2 = k'_{ab} \quad (2)$$

where $n(t)$ is the time dependent H/Pd ratio, k'_{ab} is the rate constant for hydrogen absorption, K_s is the Sievert's constant. The average hydrogen absorption rate k'_{ab}, obtained by fitting Eq. (1) to the H atom uptake regime across all experiments, reveals a markedly enhanced absorption rate in the dithiol SAM-integrated floating H_2 sensor, with an average value of $k'_{ab} = (4.6 \pm 1.1) \times 10^{-4} s^{-1}$. This is an order of magnitude higher than that of the sensor without the SAM layer ($k'_{ab} = (4.0 \pm 1.2) \times 10^{-5} s^{-1}$) (Supplementary Table S1), as shown in Fig. 3j. These results indicate that the embedded dithiol SAM effectively mitigate the substrate clamping effect, thereby facilitating hydrogen absorption. Furthermore, the inherent flexibility of dithiol molecules further promotes this process by reducing mechanical constraints at the Pd interface. As a result, the floating-structured Pd film sensor architecture design achieves significantly improved hydrogen absorption kinetics, leading to enhanced sensitivity and reduced response time during sensing operations.

Unveiling the enhanced durability of SAM-engineered H_2 Sensors

Understanding the mechanical behavior of Pd-Au heterointerfaces under tensile loading is essential for elucidating their fracture characteristics and interfacial adhesion properties. To this end, density functional theory (DFT) calculations were performed to obtain the interface binding strength and fracture behaviors of the C10 molecule incorporated Pd-Au systems. Details of the simulation procedures are provided in the Supplementary Information. Interfacial models of Pd(111)-Au(111) (Pd-Au) and Pd(111)-C10F-Au(111) (Pd-SAM-Au) were constructed with energetically stable bonding configurations, as shown in Fig. 4a. The computed interfacial binding energies indicate that the Pd-SAM-Au structure possesses a significantly lower binding energy than the Pd-Au interface (Fig. 4b), suggesting a thermodynamically more stable configuration. This enhanced interfacial adhesion is attributed to strong molecular interactions introduced by the SAM layer, as evidenced by the more negative binding energy.

To probe the mechanical integrity of the interfaces, the Pd-Au and Pd-SAM-Au systems were strained uniaxially along the z-axis until cohesive failure occurred. (Supplementary Fig. 23). The resulting stress-strain profiles are shown in Fig. 4c and Supplementary Fig. 24. For the Pd–Au interface, stress increased steadily with strain, reaching a peak at ~17%, followed by an abrupt drop, indicative of brittle fracture without significant atomic rearrangement. In contrast, the Pd-SAM-Au interface exhibited a more complex deformation behavior. Stress increased up to ~14% strain, followed by a plateau region suggesting a yielding phase. Beyond ~18%, the stress resumed rising, reaching a second peak at ~26% before final failure. This ~50% increase in fracture strain highlights the toughening effect introduced by the SAM layer, which modulates interfacial mechanics via molecular-level restructuring. The enhancement in ductility is attributed to the straightening of the SAM's initial zig-zag conformation under strain, which delays crack propagation and imparts greater mechanical resilience. As a result, the failure mode transitions from brittle to ductile upon SAM incorporation, emphasizing the pivotal role of molecular architecture in regulating interfacial fracture behavior.

To quantitatively assess the influence of the SAM buffer layer on sensor reliability, 50 repeated sensing cycles were performed under identical conditions to low (1000 ppm) and high concentration (4 vol %) of H_2, and the corresponding response curves were analyzed (Fig. 4d, e). At 1000 ppm H_2 exposure test, the sensor incorporating the SAM layer exhibited excellent repeatability, with a maximum error below 5% across all cycles. In contrast, devices lacking the SAM layer experienced a marked performance decline, showing more than 50% signal degradation after several test cycles. The difference was even more pronounced at 4 vol% H_2. Under a higher (4 vol%) H_2 concentration, some non-SAM devices failed immediately upon first exposure (Supplementary Fig. 14), highlighting their vulnerability. This contrasts with SAM-integrated devices, which showed no performance loss over 50 cycles in 1 vol% H_2, underscoring the critical role of the SAM in preventing irreversible failure (Supplementary Fig. 13). These results demonstrate that embedding a dithiol SAM at the interface substantially improves long-term operational stability by mechanically buffering the Pd–substrate interface and suppressing substrate clamping, effects that are especially critical when Pd undergoes $\alpha \rightarrow \beta$ phase transitions and large lattice expansion upon hydrogenation. In addition, the Au–SAM–Pd multilayer architecture appears to enhance H_2 adsorption/desorption kinetics in the Pd sensing layer, yielding concomitant improvements in sensitivity and response speed. Together, the data provide compelling experimental evidence that the SAM both mitigates interfacial stress and promotes faster, more reliable hydrogen sensing under practical, demanding conditions.

Sensing performance of SAM-engineered H_2 sensor

Next, the sensing performance of the floating-structured H_2 sensor incorporating a C10 SAM layer was systematically evaluated. Figure 5a shows the dynamic response curves of the sensor to H_2 concentrations ranging from 1 ppm to 4 vol% at room temperature. Notably, the sensor device achieves reliable detection of hydrogen at concentrations as low as 1 ppm and stable sensing response to high concentration of H_2 (1 vol% and 4 vol%, Supplementary Fig. 14 and Supplementary Fig. 15). Figure 5b demonstrating its suitability for trace-level monitoring in leak detection scenarios. To assess humidity tolerance, the sensor's response was measured under varying ambient RH levels at room temperature, as shown in Fig. 5c. Between 16% and 31% relative humidity (RH) the sensor exhibited a modest reduction in sensitivity and a slight slowing of response and recovery kinetics (Supplementary Fig. 16). Above 31% RH, however, both sensitivity and response/recovery times remained essentially unchanged (Fig. 5d and Supplementary Fig. 16), consistent with a saturation regime for H_2O adsorption and indicating that the floating Pd architecture mitigates humidity interference. Moreover, humidity-dependent I–V measurements show a small increase in baseline resistance (R_0) with rising RH (Supplementary Fig. 16d), suggesting weak physisorption of H_2O on Pd rather than chemisorption. This behavior is supported by H_2O adsorption-energy calculations from DFT (Supplementary Fig. 25). Additionally, cross-sensing tests confirmed the as-fabricated H_2 sensor shows high selectivity to hydrogen gas compared with other analytes, including NO_2 and H_2S (Fig. 5e), highlighting its robustness and gas-specific response. Meanwhile, long-term stability was assessed at both low and high H_2 concentrations (Fig. 5f and Supplementary Fig. 17). As shown in Fig. 5f, the sensor exhibited unnoticeable degradation in performance during a continuous testing period of over three months, maintaining consistent sensitivity and dynamic response characteristics. These results clearly demonstrate that the embedded SAM layer not only mitigates interfacial stress but also significantly enhances the operational lifetime of the device. Furthermore, the sensor device maintained stable signal output at an applied bias as low as 0.005 V, corresponding to a power consumption of ~5 μW (Fig. 5g). This ultra-low power operation renders the sensor particularly promising for large-scale integration in wireless sensor networks. Finally, a comprehensive comparison of key performance metrics, including operating temperature, detection limit, power consumption, and operational lifespan is summarized in Fig. 5h [56–65]. This comparable study demonstrated that the proposed floating-structured H_2 sensor exhibits a superior overall performance compared to previously reported H_2 sensors.

Wafer-scale fabrication of SAM-engineered H_2 sensors and test platform integration

Finally, we realized the wafer-scale fabrication of the proposed H_2 sensor and demonstrated its potential for real-time hydrogen leakage monitoring. Figure 6a shows an array of H_2 sensor devices fabricated on a 4-inch Si/SiO_2 wafer via standard photolithography processes. Each individual sensor chip was diced into 2 × 2 mm, with the C10 SAM layer selectively formed within circular regions of 200 μm diameter, over which the Pd sensing film was deposited. Detailed fabrication steps are provided in the Supplementary Information. To satisfy the requirements for practical deployment, wafer-scale fabrication of H_2 sensors must achieve both high yield and performance uniformity. To assess these metrics, 25 sensor chips were randomly selected from various regions across the wafer and characterized using a semiconductor parameter analyzer in conjunction with a probe station (Fig. 6b). The baseline resistances of all tested devices remained within 4.2 Ω, and the sensing responses to 1000 ppm H_2 exhibited minimal variation, ranging around 0.56%, thereby confirming the excellent yield and uniformity of the wafer-scale process.

https://doi.org/10.1038/s41467-026-69499-6

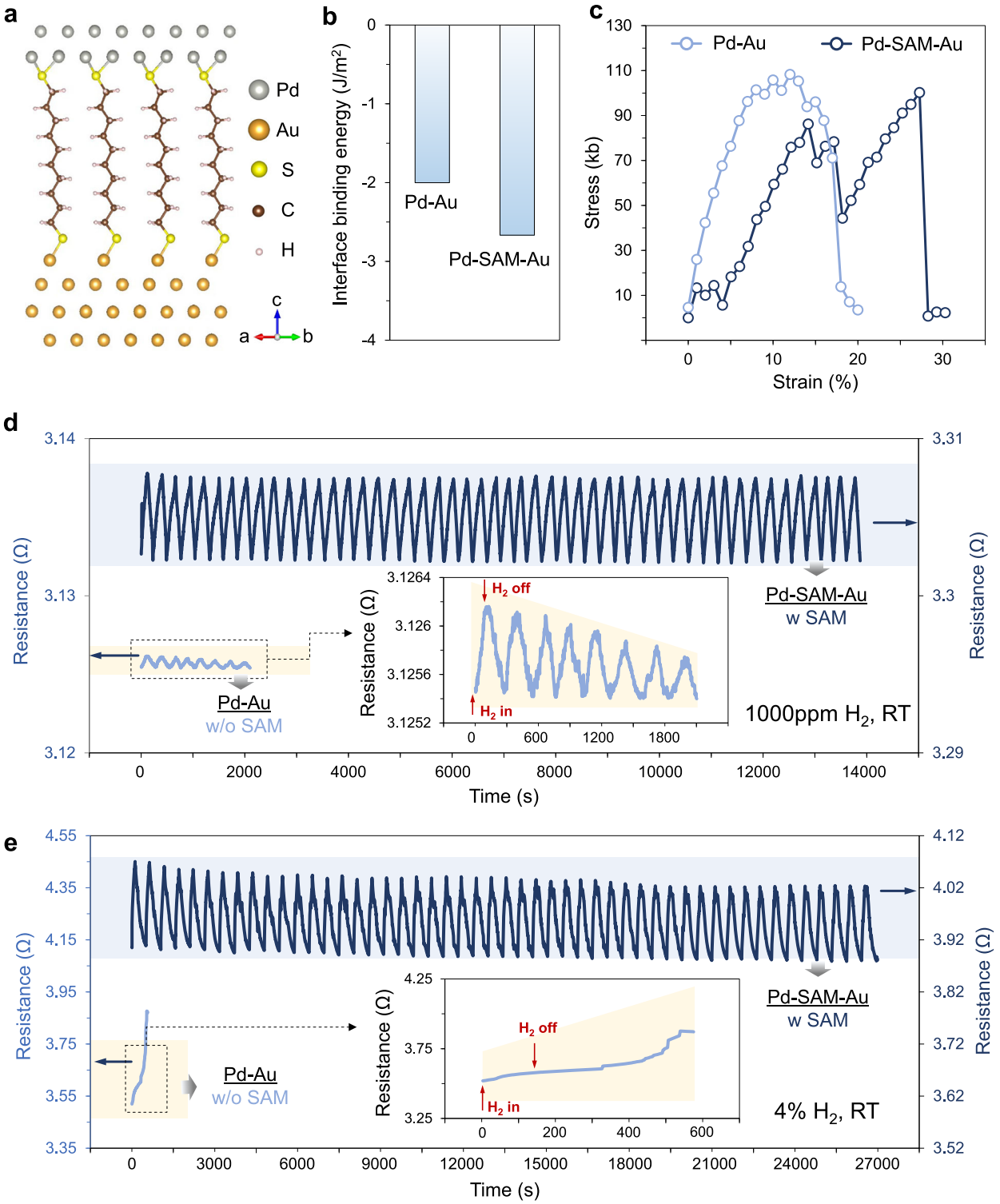

Fig. 4 | DFT modeling and experimental validation of interfacial strength and durability in the Pd–SAM–Au hydrogen sensing system. a First-principles simulated stretching model of Pd-SAM-Au interface. **b** Calculated interfacial binding energies for Pd–Au and Pd–SAM–Au configurations. **c** Stress–strain curves comparing fracture behavior of Pd–Au and Pd–SAM–Au interfaces. Experimental durability evaluation via 50 consecutive responses–recovery cycles of planar Pd–Au and floating-structured Pd–SAM–Au sensors exposed to (**d**) 1000 ppm and (**e**) 4 vol% H_2. w with, w/o without. Source data are provided as a Source Data file.

Furthermore, sensor chips were packaged using Au wire ball-bonding techniques, and the packaged devices retained nearly identical sensing responses compared to their unpackaged counterparts (Fig. 6c). This result confirms the compatibility of the proposed sensor design with standard microelectromechanical systems (MEMS) packaging processes and underscores its potential for scalable and practical applications.

Since the sensing signal generated during H_2 detection typically manifests as a weak voltage variation (on the order of tens of millivolts), signal amplification and noise suppression are critical for the

https://doi.org/10.1038/s41467-026-69499-6

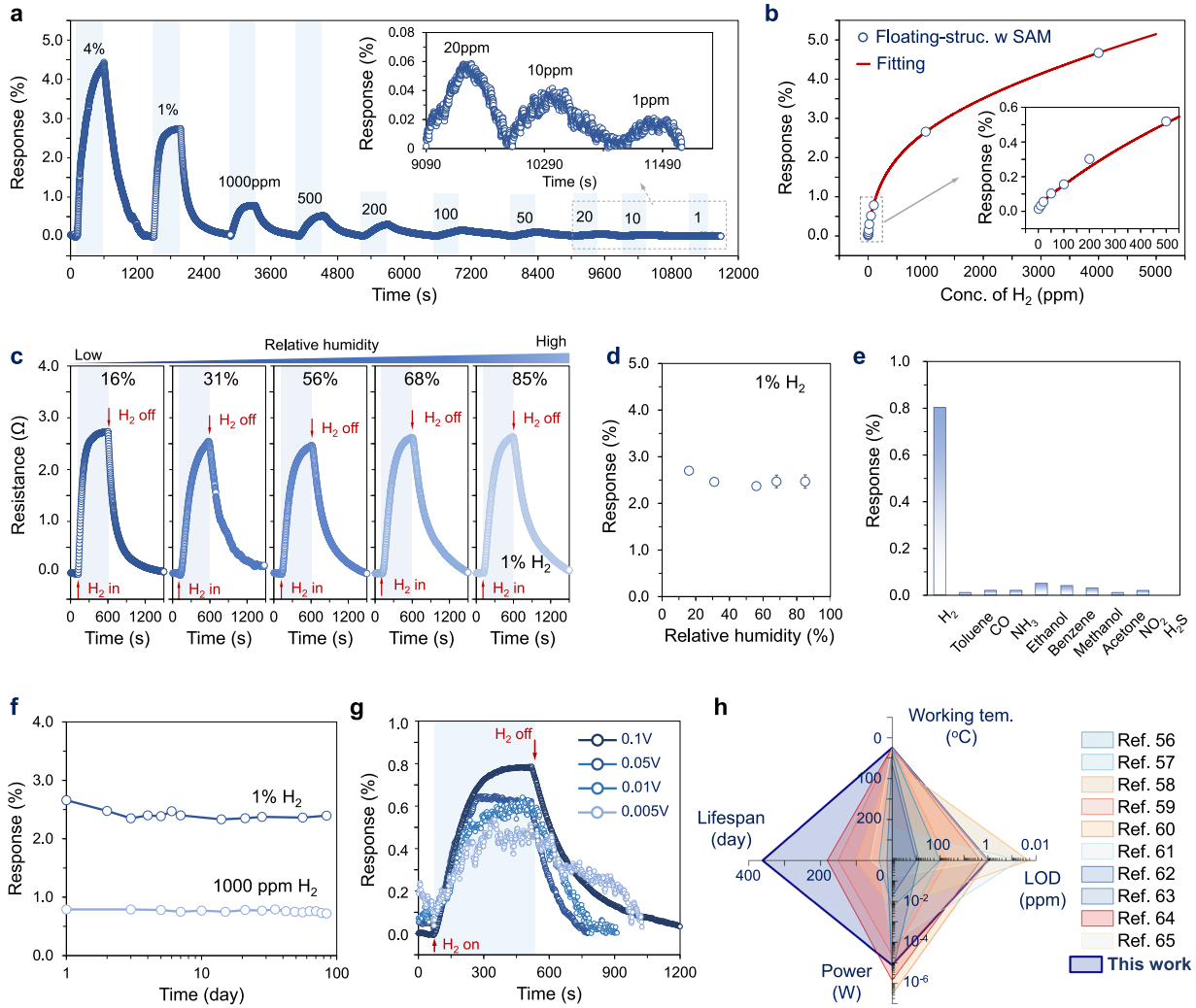

Fig. 5 | Sensing performance of the floating-structured H_2 sensor embedded with C10 SAM layer. a Dynamic response and recovery profiles across H_2 concentrations from 1 ppm to 4 vol% H_2. **b** Concentration-dependent H_2 sensitivity extracted from (**a**). The analytical fit line is based on the function $y = 2.91 \times 10^{-5}x + 0.856\ln(1.48 \times 10^{-3}x + 1.04)$, optimized using the minimum chi-square method, $r^2 = 0.999$. **c** Dynamic response and recovery profiles to 1 vol% H_2 at different humidity environment (16–85%), room temperature. and (**d**) humidity-dependent H_2 sensitivity ($n = 4$). n represents the number of technical independent replicates. The error bars represent the standard deviation of four repeated sensing cycles measured on a single sensor device. **e** Selectivity evaluation under exposure to interfering analytes. **f** Long-term operational stability under continuous 1000 ppm and 1 vol% H_2 sensing. **g** Sensor response measured at operating voltages ranging from 0.005 to 0.1 V. **h** Multi-metric performance benchmarking against state-of-the-art H_2 sensors. Struc. structure, Conc. concentration, w with, Tem. temperature, LOD limit of detection. Source data are provided as a Source Data file.

development of reliable H_2 leakage monitoring platforms. To address this, a multifunctional detection module integrating a Wheatstone bridge and an operational amplifier circuit was designed and fabricated on a printed circuit board (PCB), as illustrated in Fig. 6d. Detailed circuit schematics are provided in the Supplementary Fig. 29. Data acquisition and communication were facilitated via an analog-to-digital converter (ADC) and a microcontroller unit (MCU), powered by a 5 V regulator with integrated ON/OFF switches and GPIO interfaces. The processed sensing data was wirelessly transmitted to a smart platform through Wi-Fi for real-time feedback of environmental hydrogen concentrations (Fig. 6d). Figure 6e depicts the fully assembled hydrogen (H_2) leakage monitoring module, with its data output interfaced to a laptop for visualization. To evaluate the efficacy of the signal amplification design, we compared the sensing responses of the platform integrated with and without the Wheatstone bridge-amplifier circuit under 1000 ppm H_2 (Fig. 6f). The results revealed a three-order-of-magnitude enhancement in voltage signal amplitude upon integration of the amplification module, while maintaining excellent signal stability. Furthermore, the platform demonstrated consistent signal enhancement across a wide range of H_2 concentrations (1–1000 ppm), with a notably strong and stable response even at 1 ppm (Fig. 6g and Supplementary Fig. 30), confirming its high sensitivity and practical utility for real-time hydrogen monitoring. To extend its applicability, a handheld hydrogen leakage monitoring platform was developed by integrating the fabricated MEMS H_2 sensor with commercial temperature and humidity sensors, as illustrated in Fig. 6h. Details of the sensing platform design are provided in the Supplementary Fig. 31. Owing to its compact form factor and portability, the platform enables versatile deployment in real-time H_2 leak detection scenarios. To demonstrate a practical application, Fig. 6i shows the system operating within a hydrogen cylinder cabinet, a setting where reliable safety monitoring is needed. Leveraging an embedded H_2 concentration recognition algorithm, the platform is capable of delivering real-time feedback of ambient H_2 levels (Fig. 6j, k) and automatically triggering a leakage alarm when abnormal concentrations are detected. Furthermore, a comparative test using our integrated handheld detection

https://doi.org/10.1038/s41467-026-69499-6

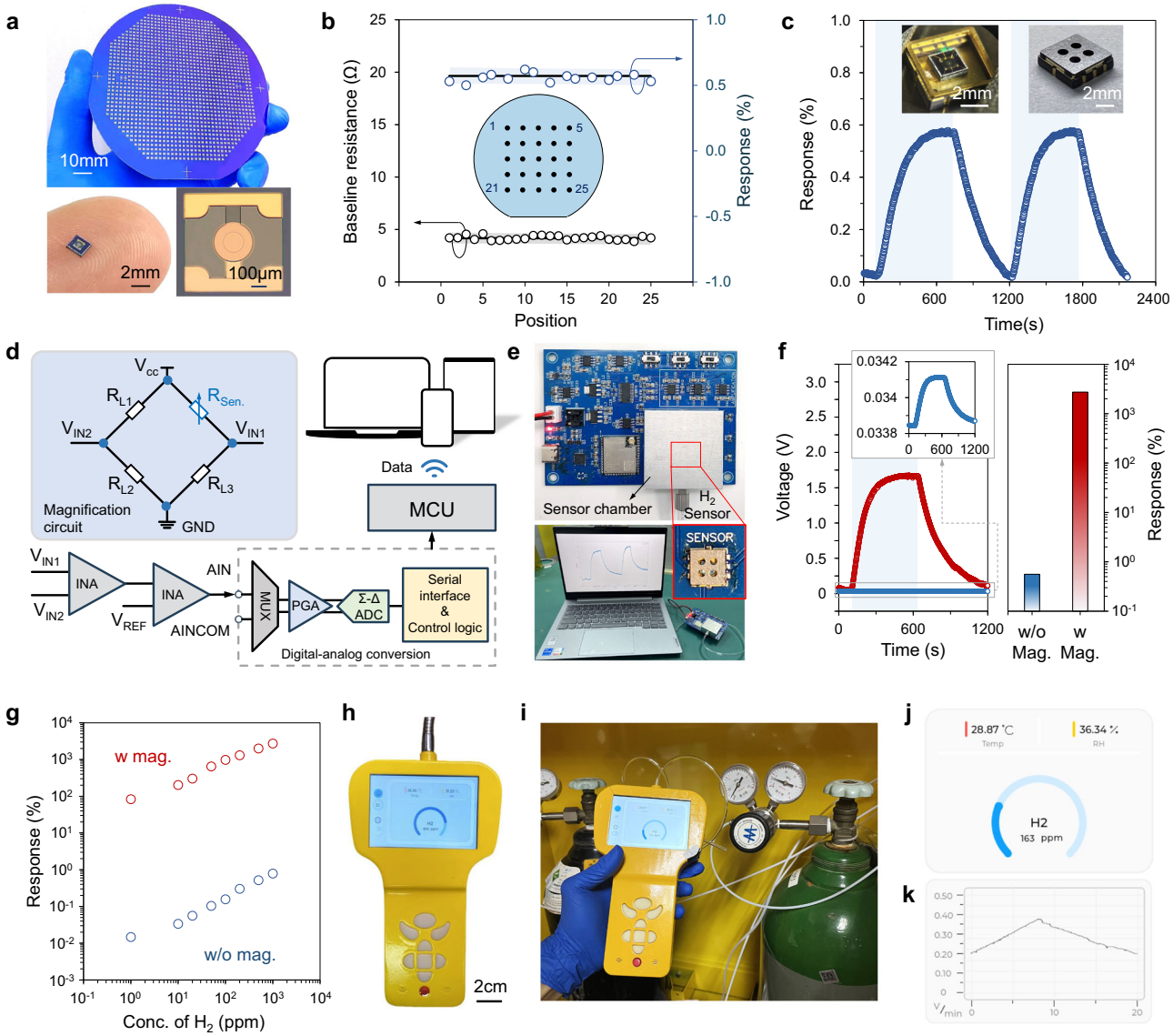

Fig. 6 | Wafer-scale fabrication of floating-structured Pd film H_2 sensor and integration of H_2 monitoring platform. a Photograph of 4-inch wafer-scale sensor arrays and singulated sensor chips. **b** Resistance measurements and H_2 sensing performance characterization of the fabricated sensor arrays. **c** Sensor packaging via ball bonding and evaluation of post-packaging sensing performance under 1000 ppm H_2. **d** Hardware architecture of the sensor signal acquisition system. **e** Wireless H_2 detection system for remote data transmission. **f** Left: Dynamic response and recovery curves of sensor platforms with and without integration of the Wheatstone bridge-amplifier circuit under 1000 ppm H_2. Right: Extracted H_2 sensitivity corresponding to the left panel. Inset (left): H_2 sensing response of the platform without the amplifier circuit. **g** Sensor response to H_2 concentrations ranging from 1 to 1000 ppm with integrated circuitry. **h** Portable hydrogen leak monitoring platform integrated with SAM-engineered sensors. **i** Field deployment of the monitoring platform for H_2 leak detection in hydrogen storage cabinets. **j**, **k** User interface for real-time monitoring of H_2 concentrations and dynamic leak detection. Conc. concentration, Mag. magnification, Sen. sensor, w with, w/o without. Source data are provided as a Source Data file.

platform and a commercially available Honeywell hydrogen detector (BWS1-R-Y) was performed (Supplementary Movie 1 and Movie 2). The results show that our sensor-integrated device was able to accurately detect and quantify the 1000 ppm H_2 sample, yielding a response comparable to that of the commercial sensor. Furthermore, our system demonstrated a faster detection response, which we attribute to the integration of a miniaturized micro-pump within the handheld unit. This active sampling route allows more rapid intake of ambient gas, thereby improving response speed compared to passive diffusion-based commercial H_2 detector. This demonstrates the practical feasibility, precision, and reliability of our system in real detection scenarios, particularly for low-concentration, pre-explosive hydrogen monitoring.

Discussion

In this work, we present a floating-structure molecular sensor designed with a mechanically reinforced heterointerface, incorporating a dithiol-terminated SAM as a molecular bridge between the Pd sensing layer and the underlying electrode for hydrogen detection. In contrast to conventional van der Waals-bonded interfaces, the engineered interface in our device leverages strong sulfur-metal coordination and a flexible carbon backbone, significantly enhancing interfacial toughness and mechanical reliability. This molecular interface not only improves structural stability but also mitigate the mechanical clamping effect from substrate and accelerates H_2 absorption kinetics. As a result, the stress-relieving architecture confirms a stable and cyclable H_2 detection at concentrations up to 4 vol%. Moreover, the sensor

achieves a gigantic improvement in sensitivity at room temperature, with a detection limit down to 1 ppm. Beyond device-level improvements, we demonstrate the feasibility of wafer-scale fabrication, yielding high device uniformity and integration potential. Leveraging this scalability, the floating-structure H_2 sensors were successfully incorporated into a portable detection module capable of real-time hydrogen leak monitoring in practical scenarios. Collectively, this work introduces a new paradigm for molecular interface design in chemical sensors, addressing the longstanding trade-off between sensitivity and mechanical durability. The integration of robust molecular anchoring with scalable fabrication strategies lays a versatile foundation for next-generation sensor systems, offering enhanced lifetime, reliability, and real-world applicability.

Methods

SAM-engineered sensor device fabrication

The fabrication process begins with the patterning of gold electrodes on a Si/SiO_2 substrate, using photolithography (ABM/6/350/NUV/SFM/SA, Incorporated company, San Jose, CA, USA). Subsequently, Cr/Au electrodes are deposited via radio-frequency magnetron sputtering (RF, ASC-5-501C, ANSEI TECH., Japan). Next, the patterning of SiO_2 insulation layer is carried out using photolithography, followed by the deposition of SiO_2 layer using RF sputtering. Afterward, photolithography is used to define the palladium (Pd) sensitive layer pattern, and the wafer is then immersed in a precursor solution to grow SAM buffer layer, and followed by the deposition of Pd layer via RF sputtering. Finally, the Pt electrode pattern is defined on the Pd-sensitive layer using photolithography, and Ti/Pt layer are deposited via RF sputtering, completing the fabrication of the hydrogen sensor.

Microstructure characterizations

The microstructure of deposited Au and Pd films were obtained using a JEOL JSM-7610F microscope. After the sensor device fabricated, a Pd-SAM-Au samples were processed by the focused ion beam method to obtain an ultrathin section of the interface, and then mounted it on grids and characterized using Transmission Electron Microscopy (TEM) (JEM-ARM200F, JOEL), with Elemental Dispersive X-ray (EDX) mapping for elemental analysis. To evaluate the chemical bonding at the SAM@Au and SAM@Pd interfaces, X-ray Photoelectron Spectroscopy (XPS) (PHI-5000 VersaProbe III, ULVAC) equipped with an argon ion sputtering system was employed. The process for fabricating the ultraviolet photoelectron spectroscopy (UPS) samples was the same as that for XPS samples. UPS measurements were conducted under a base pressure of $>2 \times 10^{-9}$ Torr, using He I (h = 21.22 eV) as the excitation source. To acquire secondary electron cutoff (SEC) data, a −10 V bias was applied to the sample in a normal emission geometry. For all UPS spectra, the Fermi level was calibrated by determining the Fermi edge of a clean Au film sputtered onto the sample, and it was set as the zero binding energy.

H_2 sensing measurement

Gas measurements were conducted by using a probe station (KT-0904T-RL, Ketan Instrument) combined with a semiconductor analyzer (4200A-SCS, Keithley). The total flow rate was maintained at a constant 1000 sccm. The test temperature was controlled at 25 °C and a ranged relative humidity from 16-85%. The mass flow controller (MFC, KT-D07-19B) was controlled via LabVIEW software, enabling precise adjustment of hydrogen concentration (1 ppm-4 vol%) by mixing hydrogen with nitrogen. Resistance of the sensor device under N_2 was recorded as baseline (R_{N2}). The resistance upon exposure of H_2 gas (Weichuang Standard Reference Gas, Shanghai) was noted as R_{gas}, and sensing response was defined as Response (%) = $[(R_{gas}\text{-}R_{N2})/R_{N2}]\times100$. The recovery time was defined as the time required for the recovery of the resistance to 90% of R_{N2} for the desorption process. All the sensing tests were carried out under a DC bias voltage of 0.1 V.

DFT calculations

The energy diagrams and strain-dependent density of state (DOS) of C10 molecule and Pd-C10-Au systems are modeled and calculated via Density functional theory (DFT) simulation. the Au-Pd and Au-SAM-Pd structures. To further investigate the mechanical properties of the interfaces, DFT calculations were applied to simulate the interface binding strength and fracture behavior of Pd-Au and Pd-SAM-Au models. Details of the simulation procedures are provided in the Supplementary Information.

Wafer-size H_2 gas sensor fabrication and package

The wafer-scale fabrication of floating-structure H_2 gas sensor are followed with a standard photolithography technique on 4-inch SiO_2/Si substrate. Specific fabrication processes are similar as the above SAM-engineered sensor device. After wafer-level fabrication, the 4-inch wafer was diced into multiple micro-nano hydrogen gas sensor chips. The sensor chips were fixed to their respective packaging using epoxy resin, and the electrodes on both ends of the chips were connected to the package pins via ball bonding. Finally, the sensor chip package was sealed using epoxy resin.

H_2 test platform integration

In the fabrication of the detection system, the circuit and PCB design were carried out using JLCPCB EDA software (JLCPCB, China). The Wheatstone bridge circuit and low-power instrumentation amplifier (AD8421BRZ, Analog Devices, USA) convert the small resistance changes caused by environmental gas variations into measurable voltage changes. These signals are then amplified in two stages and filtered to detect hydrogen at different concentrations. The voltage is sampled using an ultra-low noise ADC (AD7193BRUZ, Analog Devices, USA), which features high resolution, precision, and extremely low offset voltage, enabling accurate signal acquisition after amplification and filtering. The USB-to-UART bridge chip (CP2102-GMR, Silicon Labs, USA) and its peripheral circuitry are used for programming and driver downloading. The main controller (ESP32-S3-WROOM-1U-N4 MCU module) communicates with the ADC chip via SPI, receiving the digitized signals. This MCU module is a versatile Wi-Fi and Bluetooth Low Energy (BLE) chip, capable of transmitting the sensor signals collected by the ADC to a PC or smartphone over Wi-Fi. For power management, the system is powered by a 7.4 V lithium-ion battery (18650, Tianke Tai, China) and uses multiple linear regulators for voltage stabilization (AMS1117-3.3 V, MSKSEMI, Hong Kong; TPS7A7002DDAR, TI, USA), as well as a charge pump (TP7660H, TOPPWER, China) to generate negative voltage. These components ensure proper power supply and reference voltage for each module. Additionally, the system uses passive components (resistors, capacitors, ferrite beads, etc., in 0805 and 0603 packages), power button switches (XKB8585-Z-150, China), and sliding switches (Shouhan, MST22D18G2 125, China).

Reporting summary

Further information on research design is available in the Nature Portfolio Reporting Summary linked to this article.

Data availability

The data that support the findings of this study are available within the paper and its Supplementary Information. The Source Data used in this study are available in the Figshare database under accession code [https://doi.org/10.6084/m9.figshare.29109860]. Source data are provided with this paper.

References

1. Zhang, B. et al. A three-dimensional liquid diode for soft, integrated permeable electronics. *Nature* **628**, 84–92 (2024).
2. Matsuhisa, N. et al. High-frequency and intrinsically stretchable polymer diodes. *Nature* **600**, 246–252 (2021).

3. Choi, C. et al. Reconfigurable heterogeneous integration using stackable chips with embedded artificial intelligence. *Nat. Electron.* **5**, 386–393 (2022).
4. Wirthl, D. et al. Instant tough bonding of hydrogels for soft machines and electronics. *Sci. Adv.* **3**, e1700053 (2017).
5. Zeng, H. et al. Long-term stability of oxide nanowire sensors via heavily doped oxide contact. *ACS Sens* **2**, 1854–1859 (2017).
6. Huang, W. et al. Design of stretchable and self-powered sensing device for portable and remote trace biomarkers detection. *Nat. Commun.* **14**, 5221 (2023).
7. Wang, Z. et al. A bioinspired adhesive-integrated-agent strategy for constructing robust gas-sensing arrays. *Adv. Mater.* **33**, 2106067 (2021).
8. Guan, D. et al. Hydrogen society: From present to future. *Energy Environ. Sci.* **16**, 4926–4943 (2023).
9. Blay-Roger, R. et al. Natural hydrogen in the energy transition: Fundamentals, promise, and enigmas. *Renew. Sust. Energ. Rev.* **189**, 113888 (2024).
10. Hübert, T., Boon-Brett, L., Black, G. & Banach, U. Hydrogen sensors–A review. *Sens. Actuat. B-Chem.* **157**, 329–352 (2011).
11. Sun, B., Zhang, M., Sun, Q., Zhong, J. & Shao, G. Review on natural hydrogen wells safety. *Nat. Commun.* **16**, 369 (2025).
12. Najjar, Y. S. H. Hydrogen safety: The road toward green technology. *Int. J. Hydrog. Energy* **38**, 10716–10728 (2013).
13. Adams, B. D. & Chen, A. The role of palladium in a hydrogen economy. *Mater. Today* **14**, 282–289 (2011).
14. Favier, F., Walter, E. C., Zach, M. P., Benter, T. & Penner, R. M. Hydrogen sensors and switches from electrodeposited palladium mesowire arrays. *Science* **293**, 2227–2231 (2001).
15. Darmadi, I., Nugroho, F. A. A. & Langhammer, C. High-performance nanostructured palladium-based hydrogen sensors—Current limitations and strategies for their mitigation. *ACS Sens* **5**, 3306–3327 (2020).
16. Akiba, H. et al. Nanometer-size effect on hydrogen sites in palladium lattice. *J. Am. Chem. Soc.* **138**, 10238–10243 (2016).
17. Lee, H. S., Kim, J., Moon, H. & Lee, W. Hydrogen gas sensors using palladium nanogaps on an elastomeric substrate. *Adv. Mater.* **33**, 2005929 (2021).
18. Yin, S. et al. Hydrogen embrittlement in metallic nanowires. *Nat. Commun.* **10**, 2004 (2019).
19. Verma, N. et al. Dislocations, texture and stress development in hydrogen-cycled Pd thin films: An in-situ X-ray diffraction study. *Int. J. Hydrog. Energy* **47**, 12119–12134 (2022).
20. Yeasmin, R., Jung, G., Han, S., Park, C. & Seo, H. Self-healing and self-adhesive hydrogen gas sensing tape for robust applications. *Chem. Eng. J.* **482**, 148911 (2024).
21. Lee, J., Shim, W., Lee, E., Noh, J. S. & Lee, W. Highly mobile palladium thin films on an elastomeric substrate: Nanogap-based hydrogen gas sensors. *Angew. Chem. Int. Ed.* **50**, 5301 (2011).
22. Lee, J. et al. Cracked palladium films on an elastomeric substrate for use as hydrogen sensors. *Int. J. Hydrog. Energy* **37**, 7934–7939 (2012).
23. Kim, K. R., Noh, J.-S., Lee, J. M., Kim, Y. J. & Lee, W. Suppression of phase transitions in Pd thin films by insertion of a Ti buffer layer. *J. Mater. Sci.* **46**, 1597–1601 (2011).
24. Wu, P.-H. et al. Organosiloxane monolayers terminated with amine groups as adhesives for Si metallization. *ACS Appl. Nano Mater.* **3**, 3741–3749 (2020).
25. Othonos, A., Kalli, K. & Tsai, D. P. Optically thin palladium films on silicon-based substrates and nanostructure formation: Effects of hydrogen. *Appl. Surf. Sci.* **161**, 54–60 (2000).
26. Jeong, J. W. et al. High-resolution nanotransfer printing applicable to diverse surfaces via interface-targeted adhesion switching. *Nat. Commun.* **5**, 5387 (2014).
27. Bavili, N., Ali, B., Morova, B., Alaca, B. E. & Kiraz, A. Use of an elastic buffer layer for improved performance of a polymer microcylinder ring resonator hydrogen sensor. *Sens. Actuat. B-Chem.* **358**, 131431 (2022).
28. Johnson, N. J. J. et al. Facets and vertices regulate hydrogen uptake and release in palladium nanocrystals. *Nat. Mater.* **18**, 454–458 (2019).
29. Hong, J. et al. Metastable hexagonal close-packed palladium hydride in liquid cell TEM. *Nature* **603**, 631–636 (2022).
30. Wang, Y. et al. Piezovoltaics from PdH_x. *J. Phys. Chem. Lett.* **14**, 3168–3173 (2023).
31. Deng, Q. et al. Catalytic hydrodehydroxylation of biomass-related chemicals via water-mediated hydrogen heterolysis over a Pd–S interface. *ACS Catal.* **13**, 14356–14366 (2023).
32. Cheng, H. et al. Ligand-exchange-induced amorphization of Pd nanomaterials for highly efficient electrocatalytic hydrogen evolution reaction. *Adv. Mater.* **32**, 1902964 (2020).
33. Lau, K. H. A., Huang, C., Yakovlev, N., Chen, Z. K. & O'Shea, S. J. Direct adsorption and monolayer self-assembly of acetyl-protected dithiols. *Langmuir* **22**, 2968–2971 (2006).
34. Castner, D. G., Hinds, K. & Grainger, D. W. X-ray photoelectron spectroscopy sulfur 2*p* study of organic thiol and disulfide binding interactions with gold surfaces. *Langmuir* **12**, 5083–5086 (1996).
35. Weckenmann, U., Mittler, S., Krämer, S., Aliganga, A. K. A. & Fischer, R. A. A Study on the Selective Organometallic Vapor Deposition of Palladium onto Self-assembled Monolayers of 4, 4′-Biphenyldithiol, 4-Biphenylthiol, and 11-Mercaptoundecanol on Polycrystalline Silver. *Chem. Mater.* **16**, 621–628 (2004).
36. Schwartz, D. K. Mechanisms and kinetics of self-assembled monolayer formation. *Annu. Rev. Phys. Chem.* **52**, 107–137 (2001).
37. Bedi, A., Manor Armon, A., Diskin-Posner, Y., Bogosalvsky, B. & Gidron, O. Controlling the helicity of π-conjugated oligomers by tuning the aromatic backbone twist. *Nat. Commun.* **13**, 451 (2022).
38. Zhuo, Z. et al. Intrinsically stretchable fully π-conjugated polymer film via fluid conjugated molecular external-plasticizing for flexible light-emitting diodes. *Nat. Commun.* **15**, 7990 (2024).
39. Häkkinen, H. The gold–sulfur interface at the nanoscale. *Nat. Chem.* **4**, 443–455 (2012).
40. Gupta, R. et al. Nanoscale molecular rectifiers. *Nat. Rev. Chem.* **7**, 106–122 (2023).
41. Su, T. A., Neupane, M., Steigerwald, M. L., Venkataraman, L. & Nuckolls, C. Chemical principles of single-molecule electronics. *Nat. Rev. Mater.* **1**, 1–15 (2016).
42. Li, T., Bandari, V. K. & Schmidt, O. G. Molecular electronics: Creating and bridging molecular junctions and promoting its commercialization. *Adv. Mater.* **35**, 2209088 (2023).
43. You, S. et al. Quantifying the conductivity of a single polyene chain by lifting with an STM tip. *Natu. Commun.* **15**, 6475 (2024).
44. Merino-Díez, N. et al. Width-dependent band gap in armchair graphene nanoribbons reveals Fermi level pinning on Au (111). *ACS Nano* **11**, 11661–11668 (2017).
45. Braun, S., Salaneck, W. R. & Fahlman, M. Energy-level alignment at organic/metal and organic/organic interfaces. *Adv. Mater.* **21**, 1450–1472 (2009).
46. Chen, X. et al. A single atom change turns insulating saturated wires into molecular conductors. *Nat. Commun.* **12**, 3432 (2021).
47. Puebla-Hellmann, G., Venkatesan, K., Mayor, M. & Lörtscher, E. Metallic nanoparticle contacts for high-yield, ambient-stable molecular-monolayer devices. *Nature* **559**, 232–235 (2018).
48. Zhai, P. et al. Regulating electronic states of nitride/hydroxide to accelerate kinetics for oxygen evolution at large current density. *Nat. Commun.* **14**, 1873 (2023).
49. Gu, M. W., Lai, C. T., Ni, I. C., Wu, C. I. & Chen, C. H. Increased Surface Density of States at the Fermi Level for Electron Transport

Across Single-Molecule Junctions. *Angew. Chem. Int. Ed.* **62**, e202214963 (2023).
50. Wang, Z. et al. Role of redox centre in charge transport investigated by novel self-assembled conjugated polymer molecular junctions. *Nat. Commun.* **6**, 7478 (2015).
51. Delmelle, R. & Proost, J. An in situ study of the hydriding kinetics of Pd thin films. *Phys. Chem. Chem. Phys.* **13**, 11412–11421 (2011).
52. Delmelle, R., Michotte, S., Sinnaeve, M. & Proost, J. Effect of internal stress on the hydriding kinetics of nanocrystalline Pd thin films. *Acta Mater.* **61**, 2320–2329 (2013).
53. Verma, N., Delhez, R., van der Pers, N. M., Tichelaar, F. D. & Böttger, A. J. The role of the substrate on the mechanical and thermal stability of Pd thin films during hydrogen (de) sorption. *Int. J. Hydrog. Energy* **46**, 4137–4153 (2021).
54. Kim, G. et al. Revealing the Substrate Constraint Effect on the Thermodynamic Behaviour of the Pd–H through Capacitive-Based Hydrogen-Sorption Measurement. *Adv. Mater.* **36**, 2310333 (2024).
55. Wagner, S. & Pundt, A. Quasi-thermodynamic model on hydride formation in palladium–hydrogen thin films: Impact of elastic and microstructural constraints. *Int. J. Hydrog. Energy* **41**, 2727–2738 (2016).
56. Wu, Z. et al. Ultra-Low-Power, Extremely Stable, Highly Linear-Response Thermal Conductivity Sensor Based on a Suspended Device with Single Bare Pt Nanowire. *ACS Sens* **9**, 4721–4730 (2024).
57. Chen, Z. et al. Balancing Pd–H Interactions: Thiolate-Protected Palladium Nanoclusters for Robust and Rapid Hydrogen Gas Sensing. *Adv. Mater.* **36**, 2404291 (2024).
58. Li, J. et al. Essential role of lattice oxygen in hydrogen sensing reaction. *Nat. Commun.* **15**, 2998 (2024).
59. Rossi, A. et al. 2D Amino-Functionalized Black Phosphorus: A New Approach to Improve Hydrogen Gas Detection Performance. *ACS Appl. Mater. Interfaces* **16**, 39796–39806 (2024).
60. Tomeček, D. et al. Neural network enabled nanoplasmonic hydrogen sensors with 100 ppm limit of detection in humid air. *Nat. Commun.* **15**, 1208 (2024).
61. Yun, J., Ahn, J.-H., Moon, D.-I., Choi, Y.-K. & Park, I. Joule-Heated and Suspended Silicon Nanowire Based Sensor for Low-Power and Stable Hydrogen Detection. *ACS Appl. Mater. Interfaces* **11**, 42349–42357 (2019).
62. Hu, Q., Solomon, P., Österlund, L. & Zhang, Z. Nanotransistor-based gas sensing with record-high sensitivity enabled by electron trapping effect in nanoparticles. *Nat. Commun.* **15**, 5259 (2024).
63. Jo, M.-S. et al. Ultrafast (~0.6s), robust, and highly linear hydrogen detection up to 10% using fully suspended pure pd nanowire. *ACS Nano* **17**, 23649–23658 (2023).
64. Kim, Y. J. et al. Highly Durable Chemoresistive Micropatterned PdAu Hydrogen Sensors: Performance and Mechanism. *ACS Sens* **9**, 5363–5373 (2024).
65. Wang, R., Zhang, X., Feng, X., Zhao, F. & Wang, H. Wheatstone Bridge MEMS Hydrogen Sensor with ppb-Level Detection Limit Based on the Palladium–Gold Alloy. *ACS Sens* **9**, 6082–6091 (2024).

Acknowledgements

G.Z. acknowledges the National Natural Science Foundation of China (No. 52375148), Natural Science Foundation of Shanghai (No. 23ZR1417000), and the Sakura Science Exchange Program in Japan Science and Technology Agency (JST) (No. S2024F0200227). F.-Z.X. thanks the Science Fund for Creative Research Groups of the National Natural Science Foundation of China (No.52321002). The authors are grateful to Prof. Fuwei Zhuge at Huazhong University of Science and Technology the insightful discussion, and to Mr. Ke Chen and Miss Lanyu Ma for their assistance with additional experiments during the revision process.

Author contributions

G.Z. and F.-Z.X. conceived and supervised the project. G.Z., R.G., and F.-Z.X. prepared the manuscript. R.G. performed most of the experiments. X.W., Y.X., and L.L. performed the DFT calculations. C.Z. and Z.W. designed the circuits and fabricated smart text platform. G.Z., R.G., and F.-Z.X. contributed to the discussion and analysis of the results and manuscript written. B.Z., K.N., and T.Y. contributed to the discussion and analysis of the results. All authors discussed the results and commented on the manuscript.

Competing interests

The authors declare no competing interests.

Additional information

Supplementary information The online version contains supplementary material available at https://doi.org/10.1038/s41467-026-69499-6.

Correspondence and requests for materials should be addressed to Guozhu Zhang or Fu-Zhen Xuan.

Peer review information *Nature Communications* thanks Xuemin Zhang, and the other, anonymous, reviewer(s) for their contribution to the peer review of this work. A peer review file is available.